PHOTONICS Research

Perovskite quantum laser with enhanced population inversion driven by plasmon-induced hot electron transfer under potential shift polarization conditions

YONG PAN,* Lijie Wu, Yuan Zhang, Yihao Zhang, Jie Xu, Haixia Xie, and Jianguo Cao

College of Science, Xi'an University of Architecture and Technology, Xi'an 710055, China
Corresponding author: panyong@xauat.edu.cn

The hot electron transfer resulting in fluorescence enhancement is significantly meaningful for theory and experiment of the study on photoelectric devices. However, the laser emission based on direct hot electron transfer is difficult to realize because of the low transfer efficiency. To achieve a laser with a new-generation mechanism based on hot electron transfer, the photoelectric co-excitation is proposed for improving the efficiency of hot electron transfer. The lasing behavior at 532 nm is realized with a threshold of 5 kw cm^{-2} and 1 μA, which can be considered as the hot electron transfer resulting in population inversion enhancement. Meanwhile, the lasing output power is 0.3 mW. The hot electrons transfer process was described via the transient absorption spectrum according to the improved ground-state bleaching and excited-state absorption signal in device ON. Through comparison with the optical pump only, the quantum efficiencies of hot electron generation (HEG) and hot electron transfer (HET) were increased ~31% and 31%, respectively. Most importantly, a triple gain mode coupling device including local surface plasmon, hot electron transfer, and array oscillation was presented. Two modes of population inversion enhancement are proposed. This study can provide theoretical and experimental reference for the research of hot electron lasers and devices. © 2024 Chinese Laser Press

https://doi.org/10.1364/PRJ.515120

1. INTRODUCTION

A hot electron is an electron in a semiconductor that absorbs certain energy (such as photons, external electric field) at the excited state [1]. In recent years, the transfer of hot electrons between different materials has received remarkable attention, especially in perovskites [2], which have become the most popular semiconductor with the advantages of high optical quantum yield, flexible energy level transition combination, efficient light absorption and luminance [3–5]. Many scholars are devoted to the phenomenon of fluorescence enhancement after hot electron transfer to perovskite. Huang *et al.* [6] reported the research results on capturing hot electrons in mixed perovskite, and directly observed the migration of hot carriers in $CH_3NH_3PbI_3$ thin films by using an ultrafast transient absorption (TA) microscope with 50 nm spatial accuracy and 300 fs time resolution. The results suggested that the devices based on hot electron transfer had potential application and research value in many areas. Cho *et al.* [7] and Huang *et al.* [8] continued to report that the combination of noble metal elements with chalcogenide/perovskite materials (Ag-CrS, Ag-CsPbBr$_3$) can effectively improve the optical emission characteristics by

relying on plasmon resonance coupling effects such as metal arrays. Although these studies have achieved some breakthroughs in theory and experiment, this enhancement always stays in the fluorescence stage, which cannot drive the transfer level to realize the population inversion for direct lasing.

Low-dimensional lasers are used in communication, photonic smart chips, quantum computers, and other cutting-edge scientific fields with flexible structure, high energy efficiency, and fast modulation. The operating threshold is an important parameter. The lower the threshold, the easier it is to realize the application of laser in the field of low-dimensional devices. At present, an effective way to reduce the threshold has been developed. Bravo *et al.* [9] reported an ultralow threshold of 70 W cm^{-2} achieved by the method of up conversion materials coupling on plasmon, which proves the effect of plasmon induction on reducing the threshold. Electrically driven plasmon lasers have been realized, even though research on electrically excited plasmon is still in its infancy. Yang *et al.* [10] reported a room temperature electrically driven UV plasmonic laser with a threshold of 70.2 A cm^{-2}. Meanwhile, they revealed a mechanism of the injection of electrical carriers through the metallic

electrode of the hybrid structure. Although the above research has achieved a breakthrough in the working threshold of optically excited and electrically excited plasmon lasers, the output intensity is still low. At the same time, the methods they provide to reduce the threshold come from the changes of external materials or structure. Therefore, reducing the laser threshold directly through the changes between atoms or electrons in the device and improving the output quality still need to be further conducted.

Here, we aim to reduce the lasing threshold while improving the output quality by a different mechanism. We will try to control electrons via electrostatic induction caused by optical and electrical co-excitation, so as to improve the transfer efficiency of hot electrons, and eventually achieve the hot electron (hot-e) laser device. The hot-e device is composed of an Au nanorod array with a WGM mode, which is fabricated by a three-beam interference ablation method in experiment. The absorption, emission, and simulation of the hot-e laser device are presented. The TA spectrum of hot-e transfer and quantum efficiency are provided to confirm the enhanced transfer efficiency. Finally, the mechanism is illustrated to explain the co-excitation pumping and three-gain hot-e laser behavior. This paper can provide a theoretical basis and experimental reference for the research of quantum lasing enhancement and threshold reduction.
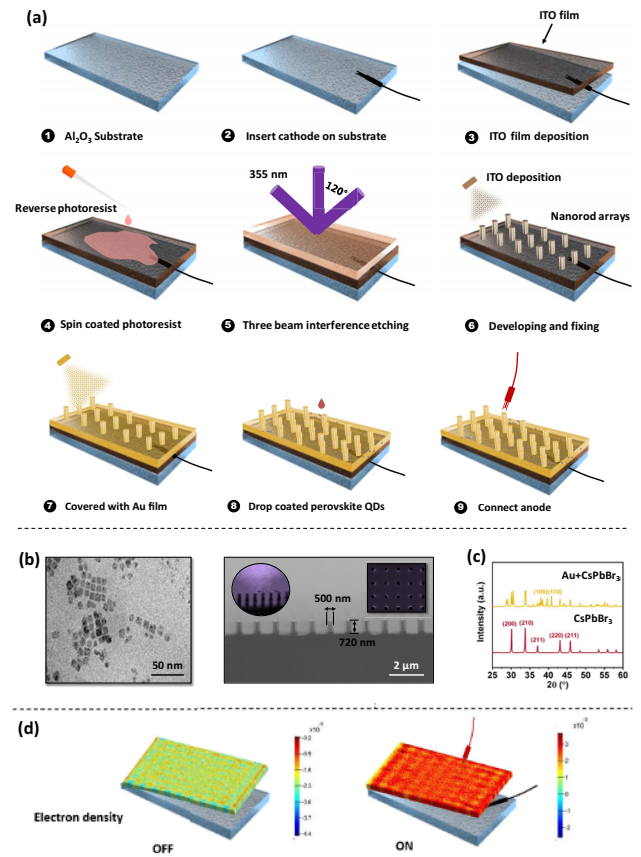
2. EXPERIMENT

A. Synthesis of CsPbBr$_3$ QDs

The thermal injection method was used to prepare CsPbBr$_3$ QDs in the experiment [11]. The synthesis of the precursor was the first step in the thermal injection. A certain amount of cesium carbonate, oleic acid, and octadecene were mixed and heated until the solution was clear and bright. Then, PbBr and octadecene were mixed and then also heated to 130° for 60 min in a three-neck flask. After first being heated, the temperature was increased continuously for about 30 min until the solution became clear. The precursor of 0.5 mL was injected into the solution. Then it was quickly put into an ice water bath for cooling. The nucleation and growth of CsPbBr$_3$ was completed within 5 s.

B. Etching CsPbBr$_3$ QDs Nanorods Array

The photoelectric co-excitation laser device can be fabricated via nine steps. The sapphire Al$_2$O$_3$ was selected as the substrate [Fig. 1(a), region 1]. The cathode electrode was pasted on the substrate first [Fig. 1(a), region 2]. Then, a thick ITO film was covered on the surface of the substrate by pulsed laser deposition (PLD) to cover the electrode [Fig. 1(a), region 3]. The details of PLD can be seen in our previous work [12]. The reverse photoresist was spined on the ITO film for etching [Fig. 1(a), region 4]. The sample was set to the three-beam interference optical path for nanorod etching [Fig. 1(a), region 5]. The details of the three-beam interference optical path can be seen in our previous work [13]. After the step of development with another ITO film deposition, the ITO nanorod arrays were obtained [Fig. 1(a), region 6]. If the positive photoresist is used, the sensitive part is removed during development and fixation. Therefore, nanohole arrays were prepared in our

Fig. 1. Experimental process, transmission electron microscope (TEM)/scanning electron microscope (SEM) image, X-ray diffraction (XRD) pattern, and electron density. (a) Experimental process of Au + CsPbBr$_3$ QDs nanorod array laser device; (b) TEM/SEM picture of CsPbBr$_3$ QDs, top view of nanorods array and cross section; (c) XRD patterns of Au + CsPbBr$_3$ and CsPbBr$_3$; (d) electron density with power ON and OFF at surface.

previous work. However, if the negative photoresist is used, the area etched by the three-beam interference spot (light-sensitive area, interference-enhanced area) is retained, and the area with reduced interference is removed. The retained pattern is a nanorod, not a nanohole. Subsequently, the nanorod array was covered by Au film for patterns transferring [Fig. 1(a), region 7]. The sample is then heated to 400°C–500°C to remove most of the photoresist. There should be about 10% photoresist in the center of the nanorod to prevent electrical short. After transfer, the CsPbBr$_3$ QDs as the gain medium were dropped on the surface of the nanorod array [Fig. 1(a), region 8]. Finally, the positive electrode can realize dynamic contact anywhere on the surface to form an electrode circuit [Fig. 1(a), region 9].

C. Characterization

The surface morphology information of the Au film, CsPbBr$_3$ QDs, and nanorod array was characterized by a scanning electron microscope (SEM, JEOLJSM 6500F). The structures of QDs were measured by XRD and Raman spectrum (Bruker D8 Advance and Horiba JobinYvon T6400). The absorption spectrum of the device was tested by a spectrometer (Hitachi, U-4100). The photoluminescence (PL) spectra were measured

by the spectrograph (NIR512 and S2000). The photonic simulation was calculated by finite-difference time-domain (FDTD) method. The TA spectrum was obtained by using a femtosecond laser (Spectra-Physics, pulse width 150 fs, 5 kHz). The detailed process of TA measurement was the same as our previous work [14]. The Keithley 2400 current source was used for testing and injection simultaneously.

3. RESULTS AND DISCUSSION

The SEM picture is displayed in Fig. 1(b). The morphology with square shape of Au + CsPbBr$_3$ QDs is presented in the left of Fig. 1(b). The average size of 10 nm is proved. The middle picture in Fig. 1(b) shows the nanorod array with the top view. The radius about 500 nm of the nanorod can be confirmed. Meanwhile, the depth of 720 nm is confirmed in the right picture of Fig. 1(b), which is decided by the exposure time in the experiment process. The film is plated after etching for a high-quality etching pattern. Furthermore, the microstructure information of Au + CsPbBr$_3$ and CsPbBr$_3$ is measured by XRD, as shown in Fig. 1(c). Compared with CsPbBr$_3$, the number of XRD peaks of Au + CsPbBr$_3$ is increased, mostly caused by Au, but does not affect the position of original peak of CsPbBr$_3$. At the same time, the cube structure is proved. In addition, the simulation of electron density was carried out through Sesita software to guide the experimental process, as shown in Fig. 1(d). A direct current with an intensity of 50 mA is generated in the simulation. The greater electron density in the state of power ON about 10 times larger than state OFF is illustrated. This means that the Au + CsPbBr$_3$ after power ON is more likely to produce electron polarization. This process is also the electrostatic induction of metal in the electric field. Under the action of the electric field, the free electrons in the neutral conductor will make directional movement and change the original charge distribution. In this process, electrons will move to the surface in a certain direction, and finally reach electrostatic balance. This also means that the surface electron density is increased. If there is a process of hot electron transfer from the metal or conductor, the transfer probability is increased.

To prove the local surface plasmon (LSP) in the metal array and the influence by current ON or OFF, the absorption of Au, CsPbBr$_3$, and Au + CsPbBr$_3$ is tested first. The absorption peaks at 496 nm, 524 nm, and 520 nm are obtained corresponding to the Au, CsPbBr$_3$, and Au + CsPbBr$_3$ (OFF), respectively [Fig. 2(a)]. The 406 nm absorption peak representing the resonance wavelength is only found in Au + CsPbBr$_3$ (OFF), which proves the LSP on the surface due to Au [7,15]. Importantly, both the resonance and absorption peak are improved by electrical power ON in Au + CsPbBr$_3$. This phenomenon suggests photoelectric excitation can produce more photon absorption, consistent with the simulation results in Fig. 1(c). Subsequently, the relationship between absorption and pump condition is studied. The lower intensity of resonance and absorption is observed at the optical pumping at 10 kW cm^{-2} and 0 μA, 100 kW cm^{-2} and 0 μA, and 100 MW cm^{-2} and 0 μA. After the current is added, the LSP resonance and absorption peak increase with the continuous increase of current from 5 kW cm^{-2} and 1 μA to

5 kW cm^{-2} and 1 mA [Fig. 2(b)]. This illustrates that the pump condition is linear for the enhancement of resonance and absorption below 1 mA current. In addition, to further prove the role of photoelectric excitation, the PL, EL, and EPL are compared in Fig. 2(c) for understanding the effect of CsPbBr$_3$ nanorod arrays. No matter how the excitation conditions change, the lasing behavior is difficult to be realized by perovskite nanorod array under 100 mW cm^{-2} and 50 mA, and only fluorescence peaks at 540 nm are found [Fig. 2(c)]. The background peak of 400–500 nm in Fig. 2(c) is caused by impurities in perovskite, and perovskite is easy to produce wide fluorescence peak under photoexcitation. At this time, the electroexcitation cannot drive the impurity to realize the transition, so it is not available under the electroexcitation condition. After the combination of perovskite and metal in Fig. 2(d), the broad fluorescence peak disappears due to the absorption of metal. At this time, the electroexcitation will cause the transfer of hot electrons, resulting in the transition of different energy levels and different fluorescence peaks. This is because the perovskite material still cannot easily realize the population inversion by itself under the action of WGM. Of course, the perovskite laser can be realized under strong excitation [16], but the threshold is too high, and the practicability is poor. Meanwhile, EL and PL of Au + CsPbBr$_3$ as the comparison group are plotted in Fig. 2(d). The narrowed PL peak can be considered as the amplified spontaneous emission (ASE) process, which still requires a larger threshold energy for laser emission. The EL spectrum shows that there is almost no luminescence. Finally, the lasing behavior at 532 nm is easily realized by optical and electrical co-excitation for Au + CsPbBr$_3$, as presented in Fig. 2(e). The emission intensity of the laser increases with the gradual increasing of electrical pump (1 μA–1 mA) at the specific optical pump (5 kW cm^{-2}). The "S" curve of the linewidth with current is plotted in Fig. 2(f), which illustrates a threshold of 5 kW cm^{-2} and 1 μA.

Furthermore, the intensity of 532 nm lasing is continuously improved as the current reaches above 1 mA. Then, the fluorescence disappears gradually with the rise of current from 1 mA to 50 mA. The change of laser is shown in the inset of Fig. 2(g). Meanwhile, the lasing behavior simulation of the device in the region −1.5–1.5 μm on the surface proceeds, as seen in Fig. 2(h). With the increasing current, the electric field intensity in the nanorod array is increased, and the intensity about 20 times higher is calculated. The variation of electric field intensity of a single nanorod is shown in the inset picture. In addition, the L-L curve and the linewidth of the emission peak as a function of pumping power are presented in Figs. 2(i) and 2(j). Nonlinear growth of output power upon the crossing lasing threshold should be obvious.

Figures 3(a) and 3(b) show the schematic diagram of the incident transverse electric (TE)- and transverse magnetic (TM)-polarized light side. TM light can excite the local surface plasmons of the array due to the structural characteristics of the nanorod. Peak splitting was performed on the extinction spectra, revealing the presence of three peaks corresponding to the response modes of the plasmon: mode 1 at 406 nm, mode 2 at 477 nm, and mode 3 at 563 nm. This work presents symmetric nondiscrete nanostructured arrays. The TE component parallel
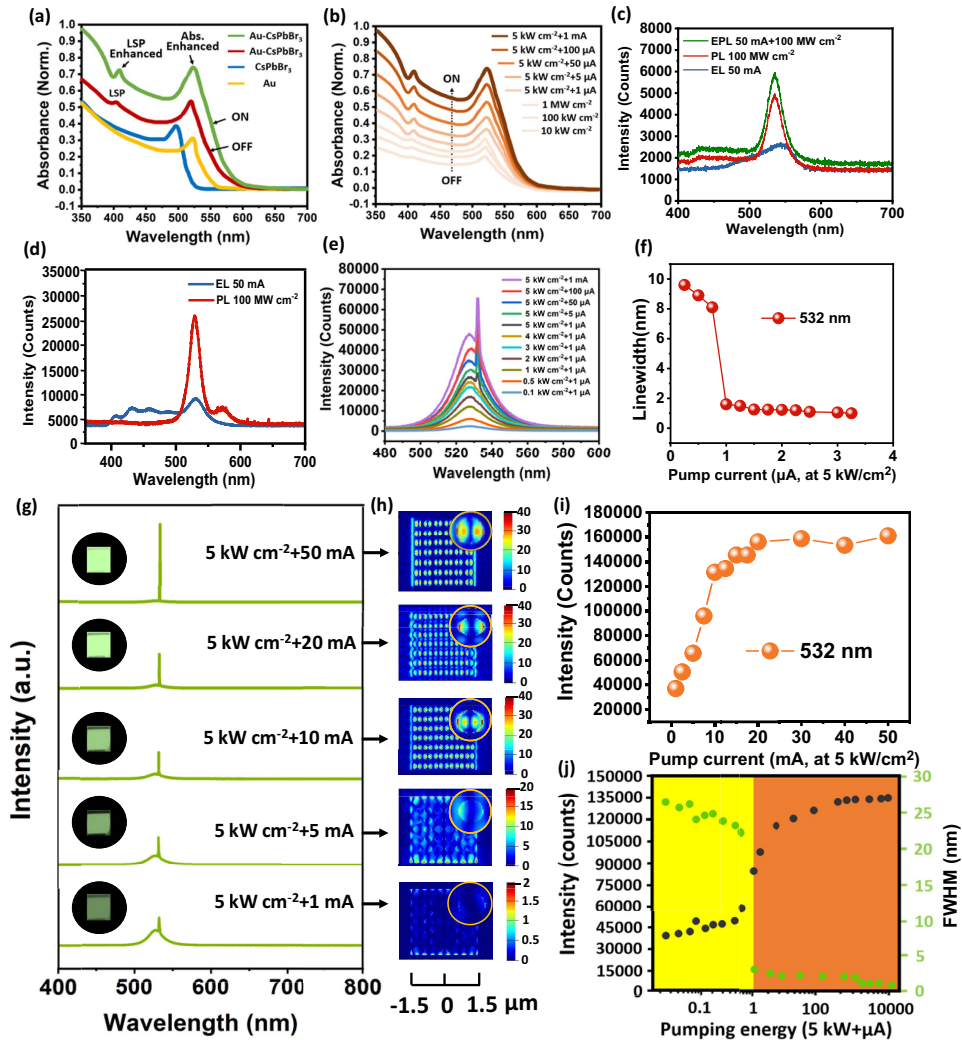
Fig. 2. Absorption, emission, and simulation of hot-e laser device. (a) Absorption spectrum of Au, CsPbBr$_3$, Au + CsPbBr$_3$ (ON), Au + CsPbBr$_3$ (OFF) at the same pump with 5 kW cm^{-2} and 1 mA; (b) absorption spectrum of Au + CsPbBr$_3$ (ON) at the different pump; (c) comparison of electroluminescence (EL), photoluminescence (PL), and electro-photoluminescence (EPL) in terms of CsPbBr$_3$; (d) comparison of EL and PL in terms of Au + CsPbBr$_3$; (e) lasing emission of the Au + CsPbBr$_3$ device in the EPL pump under 5 kW cm^{-2} and 1 mA; (f) relationship between pump current and peak linewidth; (g) lasing emission of the Au + CsPbBr$_3$ device in the EPL pump, the inset picture is the photo lasing from the device; (h) simulation of lasing process with different pump conditions in the size range –1.5–1.5 μm; (i) relationship between pump current and peak intensity; (j) L-L curve and the linewidth of the emission peak as a function of pumping power.

to the axial direction of the nanopillar will not induce a plasmonic response due to the dependence of localized surface plasmon on the size, morphology, species of metallic nanostructures, and refractive index of the external environment [17]. For mode 1, the peak at 406 nm corresponds to the absorption spectrum of Au nanostructures [Fig. 2(a)]. This demonstrates the fundamental mode response of the nanostructures to the LSPR. It also suggests that the array of nanostructures at the resonance wavelength forms an LSPR, and that this mode of the LSPR creates a stronger localized field between the nanorods. The optical extinction spectra we measured in the experiment indicate that most of the reflected light is localized in the modified mode, which reaches about 80% intensity. The mode is independent of the diffraction process of the grating, as theoretical calculations show that it does not depend on the angle of

incidence of light. Additionally, it has been demonstrated that the modified mode is the symmetric LSP mode. For mode 2, we identify the LSPR of the opposite phase of the equipartitioned excitations that couple to form a bonding mode. This bonding mode belongs to the π^*-peak of the Au nanostructure, and its spectrum should be red shifted compared to the resonance wavelength [18]. The peak data for mode 2 obtained in this work are consistent with this type. The mode could significantly enhance the localized field in the gap between the two nanorods. Therefore, this mode belongs to the coupling between two or more nanopillar plasmonic responses. For mode 3, the results of peak splitting indicate sharper peaks, which is consistent with the Fano coupling properties [19]. This position is closer to the emission peak of the spectrum, suggesting a coupling effect between the equipartitioned

excitations of the nanostructures and the nanoarray resonant cavity [20]. This confirms that when a narrowband optical resonance mode is coupled to a broadband iso-excitation resonance, the broadband iso-excitation resonance spectra will be modulated by the spectra of the narrowband optical resonance mode. This modulation, in turn, reduces the radiative damping of the LSPR. When equipartitioned exciton nanostructures are introduced into an optical microcavity system and used as an optical feedback cavity mirror, the back-and-forth oscillation process of light waves in the microcavity and the discrete exciton nanostructures can enhance the light–matter interaction, leading to more optimized photonic devices. This interaction can result in more optimized discrete exciton photonic devices. The signal regions in the transient spectrum have been marked in Figs. 3(c) and 3(d) for comparison. The ground-state bleaching (GSB) signal in Fig. 3(c) reaches $|A| = 0.4$ at 400–480 nm. When the device is on, the GSB signal strength is increased to $|A| = 1.0$, which is increased by 60%. The ground-state bleaching signal is greatly improved when the switch is on. The GSB signal indicates that the sample absorbs the pump light and then transitions to the excited state, which reduces the number of particles in the ground state. The enhancement of the GSB signal after the addition of electrical excitation indicates that it is not caused by the transition of the ground-state particles, since there is no GSB signal when there is only electrical excitation but no optical excitation [10]. Similarly, the excited-state absorption (ESA) signal (400–560 nm) and stimulated radiation (SE) signal (500–600 nm) are also improved correspondingly. The increase in the ESA signal indicates that the sample absorbs the pump light and then transitions to the excited state. Next, the particles in the excited state can absorb more light that cannot be absorbed by the original ground state and then transition to the higher excited state. This confirms the new energy brought by the hot electron transfer, otherwise it cannot prove the improvement of the ESA signal. SE signal enhancement shows that the emission is greatly enhanced [Fig. 3(d)]. Meanwhile, the hot electron transfer process also can be proved by dynamics traces, as shown in Fig. 3(e). The formula $\Delta A = \Delta A_0 + A \exp(-t/\tau)$ was used for fitting. The fitting parameters of ΔA and ΔA_0 are the TA signal intensities at times t and 0, where A is the TA amplitude ratio, and τ is the time. The signal recovers exponentially with a lifetime parameter of ~0.5 ps close to typical hot-carrier thermalization time [8] at the OFF device state, which suggests no transfer or a little transfer process. However, the multiple exponential decay components are depicted in the result of device ON (<100 fs, as limited by the instrument), which is the evidence of enhanced hot electron transfer [8,9,21,22]. One reason for enhanced transfer can be considered as the WGM in the nanorod structure. The simulation for a single nanorod is presented in Fig. 3(f). The cavity with the TM mode is presented by the electric field intensity around the rod.

Whether the transfer efficiency of hot electrons is enhanced by EPL can be directly given by the quantum efficiency (QE) test. The TA spectroscopy was used to directly measure the QE signal from the Au to CsPbBr₃ according to Refs. [21,22]. The QEs of hot electron generation (HEG) in Au and hot electron transfer (HET) to $CsPbBr_3$ can be considered as the evaluation
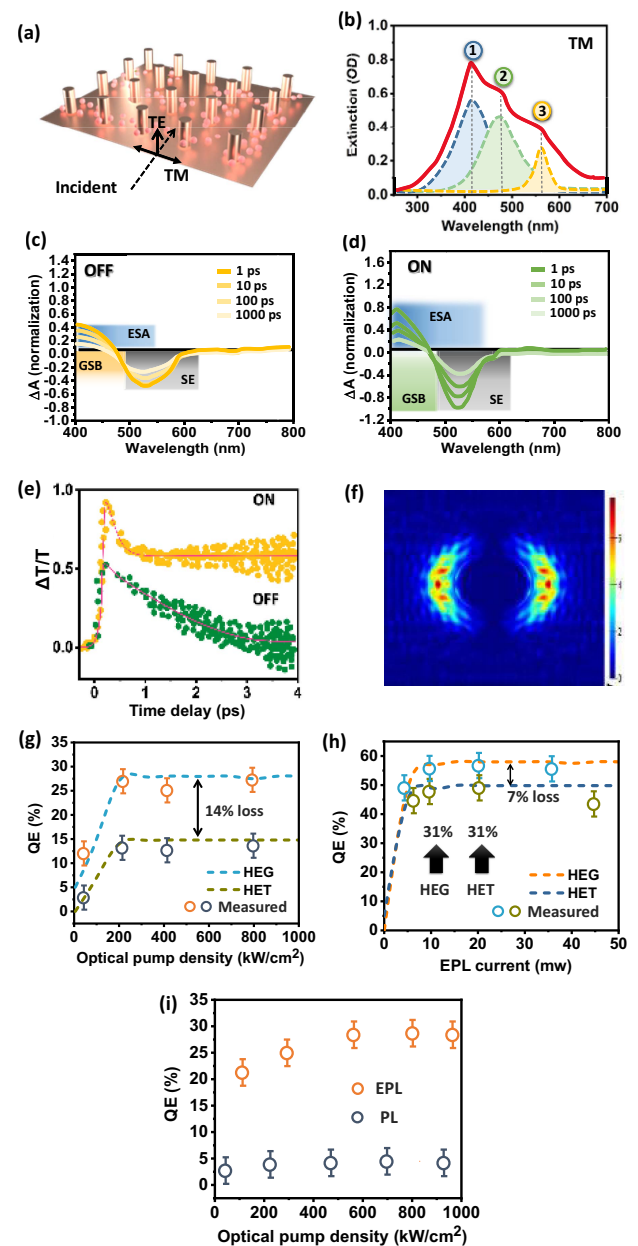
Fig. 3. TA and QE information in the Au + CsPbBr₃ EPL device. (a) Polarization analysis of three-dimensional metal nanostructures; (b) extinction spectrum of metal nanostructures measured as TM-polarized light is normal incidence; (c) TA data recorded with the LSP wavelength of 406 nm with device OFF; (d) TA data recorded with the LSP wavelength of 406 nm with device ON; (e) TA dynamics at the wavelength 406 nm with device ON and OFF; (f) simulation of single Au + CsPbBr₃ nanorod with TM mode; (g) QEs of HEG and HET of the device OFF; (h) QEs of HEG and HET of the device ON; (i) comparison of plasmon-induced hot electron generation efficiency of PL and EPL.

basis. The total plasmon-induced hot electron generation efficiency is proportional to the product of hot electron generation efficiency and hot electron transfer efficiency. This relationship can be expressed by $QE_{PI-HEG}(R) \propto QE_{HEG}QE_{HET}$. The HEG and HET can be expressed by the following formula [20,21]:

$$QE_{HEG}(R) \propto \frac{\gamma_s(R)}{\gamma_t(R)}, \qquad (1)$$

$$QE_{HET}(R) = \alpha(R) \frac{(\hbar\omega - E_b(R))^2}{\hbar\omega}, \qquad (2)$$

where $\gamma_t(R)$ is the total plasmon dephasing rate, $\gamma_s(R)$ is the additional surface dephasing rate, α is the competition factor, $\hbar\omega$ is the photon energy, and E_b is the barrier height, which is determined by the energy difference between the semiconductor conduction band edge and the Fermi level in metal. Both the measurement and simulation are plotted in Figs. 3(g) and 3(h) corresponding to the optical pumping and optical and electrical pumping. In Fig. 3(g) for optical pumping, the stable QEs of HEG of 28% and 25.5% and QEs of HET of 14% and 13.8% are obtained in simulation and measurement, respectively. The loss of 14% is illustrated from hot electrons generation to transfer. Homologous in Fig. 3(h) in terms of optical and electrical pumping, the stable QEs of HEG of 56% and 55.3% and QEs of HET of 49% and 47.5% are obtained in simulation and measurement, respectively. The loss of 7% is illustrated from hot electrons generation to transfer. Compared to optical pumping, the QEs of HEG and HET are increased about 31%, and the QEs of HEG and HET are improved by EP pump by about 2.2 and 3.5 times, which suggests the co-excitation can promote the formation of population inversion and the enhancement of laser emission effectively. The plasmon-induced hot electron transfer is proportional to the product QEs of HEG and HET [Fig. 3(i)]. The comparison with Refs. [10,15,23–28] of plasmonic nanolasers in terms of threshold and output power can be seen in Table 1.

The true evidence would be generated PL in the materials when pumping with light below its bandgap as a large number of below-bandgap photons would still be able to create high-energy electrons.

Thus, the 808 nm excitation is adopted for more concrete evidence, as seen in Fig. 4(a). The fluorescence emission at 532 nm is confirmed under 808 nm excitation, which further proved the hot electron transfer emission.
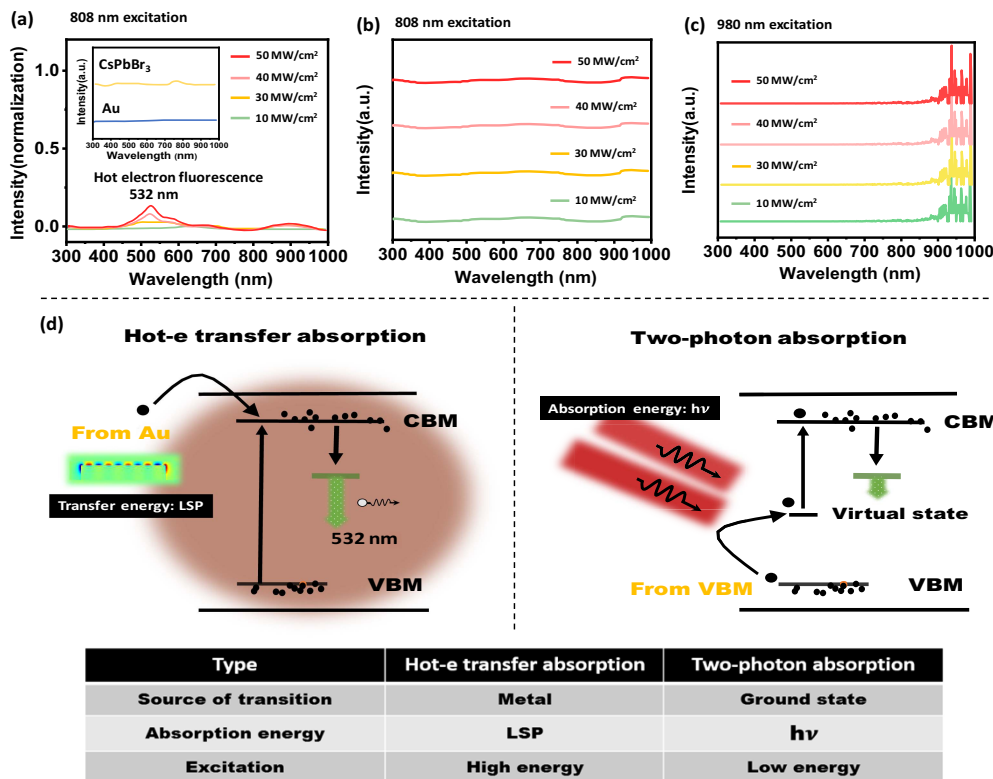
Furthermore, if there is a process of two-photon absorption and photoluminescence, the perovskite QDs in the nanorod structure should have two-photon fluorescence when we remove the Au film and PL measurement again with the same conditions. In fact, the PL results show that there is no two-photon fluorescence. To further prove the elimination of two-photon absorption, the PL spectra of $CsPbBr_3$ without Au

under 808 nm and 980 nm excitations are provided [Figs. 4(b) and 4(c)]. The results show no PL signal generation near 520 nm for $CsPbBr_3$ alone under two long-wavelength excitations with different power densities, further demonstrating the non-two-photon absorption effect. To clearly distinguish the difference between hot electron absorption and two-photon absorption, the difference between the two absorption modes is listed in Fig. 4(d). Generally, the two-photon state in the quantum dot is generated in two ways. One way is that the quantum dot simultaneously absorbs two photons with energy greater than or equal to the quantum dot band gap energy, and the other way is to absorb a photon with at least twice the quantum dot band gap energy. Importantly, the two-photon absorption mainly occurs at the focus of the super-intense laser produced by the pulse laser. The laser intensity in other places on the optical path is not enough to generate two-photon absorption. The corresponding single-photon process cannot occur due to the long wavelength and low energy of the light used.

The comparison analysis of optical pumping and optical and electrical pumping is discussed, as shown in Fig. 5(a). Under the condition of only optical pumping, the nanorod array is excited to produce LSP on its surface. The hot electrons in the nanorod will transfer to the gain material perovskite under the induction of this resonance. Among the hot electrons above the Fermi level, only a portion of them have the required energy and momentum to cross the metal/semiconductor interface to realize transfer on the conduction band (CB) in the semiconductor, which can be accounted by Fowler's model [29]. However, these slight transfers may achieve fluorescence enhancement [7,8], but they are not enough for forming and emitting a laser. The reason for this difficulty can be explained by the irregular charge distribution. A large number of charge distributions in metals are irregular, that is, only some electrons on the surface will be transferred after being induced by excitons. If this charge distribution can be regulated, the purpose of enhancing the efficiency of hot electron transfer can be realized. Therefore, the electrical pump is added for adjusting the charge distribution in metal (electrostatic induction). Under the action of the electric field, metal will produce electron polarization, which will lead to the regular distribution of electrons or charges [29]. At this time by adding an optical excitation, a large number of electrons with certain kinetic energy and regular distribution at the boundary can be transferred after receiving plasmon resonance induction. We also verify this opinion through simulation. In the case of electric field absence, only

Table 1. Comparison of Parameters in Different Plasmonic Nanolasers

Year	Wavelength	Pump	Threshold	Output Power	Ref.
2009	489 nm	Optical	40 MW cm^{-2} (<10 K)	10 nW	[23]
2012	1520 nm	Optical	100 kW cm^{-2}	10 nW	[24]
2018	700 nm	Optical	3.5 mW	1.13 mW	[25]
2019	396 nm	Electrical	70.2 A cm^{-2}	30 μW	[10]
2020	1550 nm	Electrical	47 kA cm^{-2}	100 μW	[26]
2021	530 nm	Optical	138 MW cm^{-2}	/	[15]
2022	1550 nm	Electrical	1.2 mW	0.6 mW	[27]
2023	340–360 nm	Optical	12 kW cm^{-2}	/	[28]
2024	532 nm	Optical + electrical	5 kW cm^{-2} & 1 μA	0.3 mW	This work

Type	Hot-e transfer absorption	Two-photon absorption
Source of transition	Metal	Ground state
Absorption energy	LSP	$h\nu$
Excitation	High energy	Low energy

Fig. 4. PL spectrum of CsPbBr$_3$ with and without Au under 808 nm/980 nm excitation. (a) Emission of hot electron transfer fluorescence from metal to CsPbBr$_3$; (b) PL spectrum of CsPbBr$_3$ without Au under 808 nm excitation; (c) PL spectrum of CsPbBr$_3$ without Au under 980 nm excitation; (d) comparison of hot-e absorption and two-photon absorption.

plasmons resonating on the side of the nanorod are found. However, the electron polarized LSPs are generated when the electric field is added in the Y direction.

Clearly, only relying on the transfer of hot electrons to form a laser is not enough. Here, we present a triple gain coupling device including LSP, hot-e, and array, as shown in Fig. 5(b). The LSP is generated at the initial stage under optical and electrical co-excitation, which is the first gain. Then, the second gain of hot-e transfer is induced by LSP for energy level enhancement. Finally, the LSP and hot-e are further cycle strengthened via the third gain of the array WGM-like mode in the nanorod array. Considering the refractive index of metal for excitation and the inhomogeneity of perovskite quantum dots around the Au nanorod, the generation of laser is not caused by a single nanorod WGM. Because a single metal nanorod cannot completely limit light around the nanopillar, light may surround many nanorods, which is different from the traditional WGM. Thus, we really cannot attribute the mechanism of laser generation to WGM. After the triple gain, the laser emission with low threshold and high intensity can be realized, which is also realized in the simulation. The lasing behavior in the nanorod array is photographed in real time via a micro-area spectrometer under UV excitation. The array WGM-like mode can be directly seen from Fig. 5(c). The information of hot-e transfer behavior in the energy level is depicted in Fig. 5(d). The weak light emission is generated under the condition of only optical pump. Importantly, a large

number of hot electrons can be transferred from metal Au to the CB or valence band (VB) in semiconductor CsPbBr$_3$, resulting in the 532 nm lasing emission enhancement. For more proof, the evidence of lasing interference can be seen in the right of Fig. 5(d). The output power of 0.3 mW was checked by a spot quality analyzer and a power meter, as seen in Fig. 5(d) and Table 1.

The injection of hot electrons to a designated energy level leads to an elevation in the energy gap between the two levels. This elevation can be estimated as a discrete number of inversion states. Two modes can be implemented to enhance this property, as shown in Fig. 5(e). The first mode involves occupying the high energy state with hot electrons, thereby rendering no vacancies in the high energy state for electrons in the ground state [6,9,15,30]. Consequently, a cohort number of inversion states are formed. In the second mode, a significant transfer of electrons from the metal occupying the excited-state energy levels occurs. This results in the consumption of possible energy for hot electrons due to pressure difference, which triggers ground-state electron absorption, and generates more leaps for fast and low-consumption colony number inversion [6,15,31].

According to the literature reported [32], the work function of Au is about ~4.78 eV. Therefore, the electron energy after overflow must be lower than 4.77 eV due to the loss in this process. When a metal contacts a semiconductor, its Fermi energy level will be aligned. Therefore, the transferred semiconductor energy level should be in this range. Because
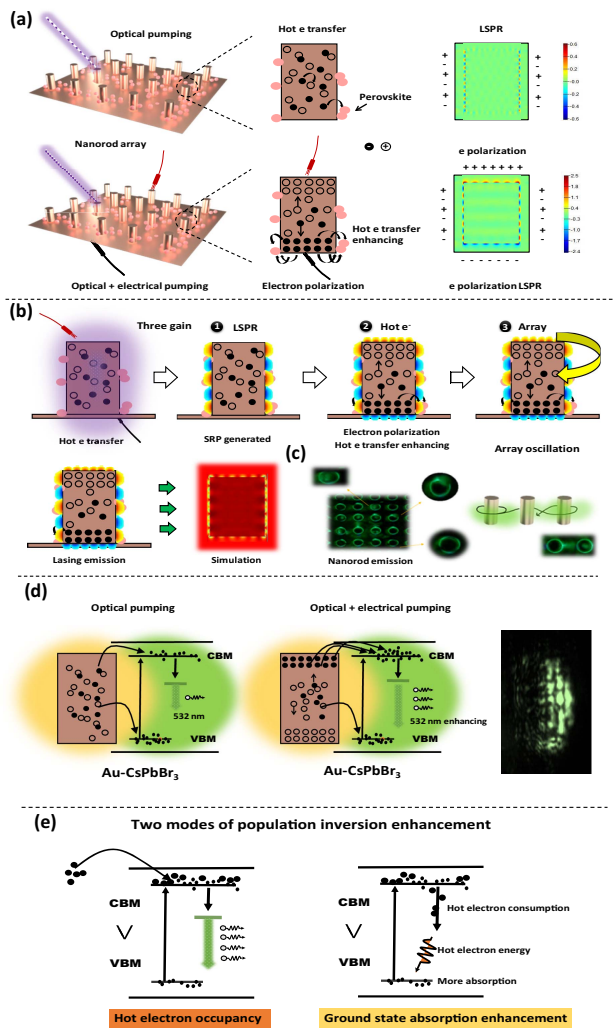
Fig. 5. Hot electron transfer mechanism analysis of electrical and optical co-excitation pumping. (a) Electron changing in nanorod under optical pumping and optical and electrical pumping; (b) process of lasing emission with three gains; (c) microscope picture of lasing emission with WGM in the nanorod array; (d) lasing enhancement analysis in the energy level of Au-CsPbBr$_3$ under two different pumping; (e) two modes of population inversion enhancement.

the energy levels of quantum dots are discrete, electrons will emit light of specific wavelength when they transition between these energy levels. Therefore, there must be an energy level in quantum dots that can be aligned with the Fermi energy level of the metal. According to the reports in Ref. [33], the energy level of –PbBr$_3$ as the luminescent center ranges from –2 to 4 eV. The 532 nm emission reported in our paper is consistent with that reported reference (532 nm is approximately equivalent to 2.33 eV).

4. CONCLUSION

In summary, we demonstrate a method of photoelectric co-excitation for 532 nm lasing based on hot electron transfer in Au-CsPbBr$_3$ via population inversion enhancement. The nanorod array with radius of 500 nm and depth of 720 nm was

obtained by three-beam pulsed laser ablation combined with PLD. The LSP in Au-CsPbBr$_3$ under photoelectric co-excitation is proved by the absorption spectrum in the steady state. Thus, the lasing behavior at 532 nm was realized with a threshold of 5 kW cm^{-2} and 1 μA. The lasing output power is 0.3 mW, which suggests that the method proposed in this paper can improve the output quality while lowering the threshold. For details, the hot electrons transfer process is described by the TA spectrum according to the improved GSB and ESA signal in device ON. Meanwhile, the multiple exponential decay components are also evidence for hot-e transfer. Through comparison with only optical pumping, the QEs of HEG and HET are increased about 31% and 31%, and the QEs of HEG and HET are improved by optical and electrical co-excitation about 2.2 and 3.5 times, respectively. This suggests the co-excitation can effectively promote the formation of population inversion and laser emission. Efficient hot electron transfer comes from the charge regulation of metals by adding an electric field. Most importantly, a triple gain coupling device including LSP, hot-e, and array WGM-like mode is presented in experiment and simulation. Finally, two modes of population inversion enhancement are proposed, including the hot electron occupancy mode and ground-state absorption enhancement mode. This work could be a theoretical basis and experimental reference for research into quantum laser enhancement and threshold reduction.

Disclosures. The authors declare that they have no competing interests.

Data Availability. Data underlying the results presented in this paper are not publicly available at this time but may be obtained from the authors upon reasonable request.

REFERENCES

1. C. H. Cho, C. O. Aspetti, J. Park, *et al.*, "Silicon coupled with plasmon nanocavities generates bright visible hot luminescence," Nat. Photonics **7**, 285–289 (2013).
2. K. Y. Jeong, M. S. Hwang, J. Kim, *et al.*, "Recent progress in nanolaser technology," Adv. Mater. **32**, 2001996 (2020).
3. R. M. Ma and R. F. Oulton, "Applications of nanolasers," Nat. Nanotechnol. **14**, 12–22 (2019).
4. Y. Pan, Y. Zhang, J. G. Cao, *et al.*, "Threshold reducing via micro rhombic lasing misalignment step-cavity with a simple and universal use," Adv. Opt. Mater. **12**, 2301877 (2023).
5. Y. L. Chen, Y. H. Hu, X. Yang, *et al.*, "Plasmon-enhanced fluorescence of gold nanoparticle/graphene quantum dots for detection of Cr^{3+} ions," Photonics Res. **11**, 1781–1790 (2023).
6. Z. Guo, Y. Wan, M. Yang, *et al.*, "Long-range hot-carrier transport in hybrid perovskites visualized by ultrafast microscopy," Science **356**, 59–62 (2017).
7. C. H. Cho, C. O. Aspetti, M. E. Turk, *et al.*, "Tailoring hot-exciton emission and lifetimes in semiconducting nanowires via whispering-gallery nanocavity plasmons," Nat. Mater. **10**, 669–675 (2011).

8. X. Y. Huang, H. B. Li, C. F. Zhang, *et al.*, "Efficient plasmon-hot electron conversion in Ag–CsPbBr$_3$ hybrid nanocrystals," Nat. Commun. **10**, 1163 (2019).

9. A. F. Bravo, D. Wang, E. S. Barnard, *et al.*, "Ultralow-threshold, continuous-wave upconverting lasing from subwavelength plasmons," Nat. Mater. **18**, 1172–1176 (2019).

10. X. Yang, P. N. Ni, P. T. Jing, *et al.*, "Room temperature electrically driven ultraviolet plasmonic lasers," Adv. Opt. Mater. **7**, 1801681 (2019).

11. Y. L. Chen, Y. H. Hu, L. Ma, *et al.*, "Self-assembled CsPbBr$_3$ quantum dots with wavelength-tunable photoluminescence for efficient active jamming," Nanoscale, **14**, 17900 (2022).

12. Y. Pan, L. Huang, W. Sun, *et al.*, "Invisibility cloak technology of anti-infrared detection materials prepared using CoGaZnSe multilayer nanofilms," ACS Appl. Mater. Interfaces **13**, 40145–40154 (2021).

13. Y. Pan, L. Wang, X. Su, *et al.*, "Nanolasers incorporating Co$_x$Ga$_{0.6-x}$-ZnSe$_{0.4}$ nanoparticle arrays with wavelength tunability at room temperature," ACS Appl. Mater. Interfaces **13**, 6975–6986 (2021).

14. Y. Pan, L. Wang, Y. Zhang, *et al.*, "Multi-wavelength laser emission by hot-carriers transfers in perovskite-graphene-chalcogenide quantum dots," Adv. Opt. Mater. **10**, 2201044 (2022).

15. D. Xing, C. Lin, P. Won, *et al.*, "Metallic nanowire coupled CsPbBr$_3$ quantum dots plasmonic nanolaser," Adv. Funct. Mater. **31**, 2102375 (2021).

16. A. P. Schlaus, M. S. Spencer, and X. Y. Zhu, "Light–matter interaction and lasing in lead halide perovskites," Acc. Chem. Res. **52**, 2950–2959 (2019).

17. X. F. Fan, W. T. Zheng, and D. J. Singh, "Light scattering and surface plasmons on small spherical particles," Light Sci. Appl. **3**, e179 (2014).

18. S. Sheikholeslami, Y. Jun, P. K. Jain, *et al.*, "Coupling of optical resonances in a compositionally asymmetric plasmonic nanoparticle dimer," Nano Lett. **10**, 2655–2660 (2010).

19. A. E. Miroshnichenko, "Fano resonances in nanoscale structures," Rev. Mod. Phys. **82**, 2257–2298 (2010).

20. H. M. Zhang, S. F. Chen, and D. W. Zhao, "Surface-plasmon-enhanced microcavity organic light-emitting diodes," Opt. Express **22**, A1776–A1782 (2015).

21. Y. Liu, Q. Chen, and D. A. Cullen, "Efficient hot electron transfer from small Au nanoparticles," Nano Lett. **20**, 4322–4329 (2020).

22. K. Wu, J. Chen, J. R. Mcbride, *et al.*, "Efficient hot-electron transfer by a plasmon-induced interfacial charge-transfer transition," Science **349**, 632 (2015).

23. R. F. Oulton, V. J. Sorger, T. Zentgraf, *et al.*, "Plasmon lasers at deep subwavelength scale," Nature **461**, 629–632 (2009).

24. M. Khajavikhan, A. Simic, M. Katz, *et al.*, "Thresholdless nanoscale coaxial lasers," Nature **482**, 204–207 (2012).

25. S. Wang, H. Z. Chen, and R. M. Ma, "High performance plasmonic nanolasers with external quantum efficiency exceeding 10%," Nano Lett. **18**, 7942–7948 (2018).

26. D. Y. Fedyanin, A. V. Krasavin, A. V. Arsenin, *et al.*, "Lasing at the nanoscale: coherent emission of surface plasmons by an electrically driven nanolaser," Nanophotonics **9**, 3965–3975 (2020).

27. A. Fattah, A. M. Livani, and E. Norouzi, "Design and simulation of an electrically pumped SPASER," Opt. Mater. **129**, 112530 (2022).

28. J. Y. Sun, D. H. Nguyen, J. M. Liu, *et al.*, "On-chip monolithically integrated ultraviolet low-threshold plasmonic metal–semiconductor heterojunction nanolasers," Adv. Sci. **10**, 2301493 (2023).

29. R. H. Fowler, "The analysis of photoelectric sensitivity curves for clean metals at various temperatures," Phys. Rev. **38**, 45–56 (1931).

30. Y. Liang, C. Li, Y. Huang, *et al.*, "Plasmonic nanolasers in on-chip light sources: prospects and challenges," ACS Nano **14**, 14375–14390 (2020).

31. G. Li, B. Zhou, Z. Hou, *et al.*, "Transfer printing of perovskite whispering gallery mode laser cavities by thermal release tape," Nanoscale Res. Lett. **17**, 8 (2022).

32. G. Kumar, M. Sarathbavan, Y. Sivalingam, *et al.*, "Mechanism of analog bipolar resistive switching and work function in Au/Na$_{0.5}$Bi$_{0.5}$TiO$_3$/Pt heterostructure thin films," Mater. Chem. Phys. **257**, 123765 (2021).

33. R. Chen, X. Su, J. Wang, *et al.*, "The roles of surface defects in MAPbBr$_3$ and multi-structures in MAPbI$_3$," Opt. Mater. **122**, 111600 (2021).